

Theory of moiré magnetism and multi-domain spin textures in twisted Mott insulator - semimetal heterobilayers

M. A. Keskiner,^{*,†} Pouyan Ghaemi,^{*,‡,¶} M. Ö. Oktel,^{*,†} and Onur Erten^{*,§}

[†]*Department of Physics, Bilkent University, Ankara, 06800, TURKEY*

[‡]*Physics Department, City College of the City University of New York, NY 10031, U.S.A.*

[¶]*Physics Program, Graduate Center of City University of New York, NY 10031, U.S.A.*

[§]*Department of Physics, Arizona State University, Tempe, AZ 85287, USA*

E-mail: akif.keskiner@bilkent.edu.tr; pghaemi@ccny.cuny.edu; oktel@fen.bilkent.edu.tr;
onur.erten@asu.edu

KEYWORDS: moiré superlattices, 2D magnets, multi-domain magnetic order.

Abstract

Motivated by the recent experimental developments in van der Waals heterostructures, we investigate the emergent magnetism in Mott insulator - semimetal moiré superlattices by deriving effective spin models and exploring their phase diagram by Monte Carlo simulations. Our analysis indicates that the stacking-dependent inter-layer Kondo interaction can give rise to different types of magnetic order, forming domains within the moiré unit cell. In particular, we find that the AB (AA) stacking regions tend to order (anti)ferromagnetically for an extended range of parameters. The remaining parts of the moiré unit cell form ferromagnetic chains that are coupled anti-ferromagnetically. We show that the decay length of the Kondo interaction can control

the extent of these phases. Our results highlight the importance of stacking-dependent interlayer exchange and the rich magnetic spin textures that can be obtained in van der Waals heterostructures.

Kondo model is a quintessential strongly-correlated model that describes the interaction between localized magnetic moments and weakly-interacting conduction electrons via an antiferromagnetic spin-spin interaction.¹⁻³ Commonly utilized for lanthanide and actinide intermetallic compounds, the Kondo model can possess diverse phenomena such as heavy fermion formation, magnetic order, and unconventional superconductivity.¹ Unlike other interacting models, such as the Hubbard model, the Kondo model exhibits a clear separation between the localized and the itinerant degrees of freedom, which allows for controlled calculations in certain limits.² In the simplest form, the Kondo model involves only local interactions since both the localized moments and the conduction electrons originate from the f and d orbitals of the same lanthanide/actinide ions in most intermetallics.

Recently, an alternative route to realize the Kondo model has emerged in van der Waals (vdW) heterostructures. These synthetic Kondo lattices consist of a two-dimensional (2D) Mott insulator layer and a metallic or semimetallic layer as depicted in Fig. 1(a,b). This route separates the Kondo model's two necessary degrees of freedom into different layers, in contrast to the intermetallics. For instance, a synthetic Kondo lattice has been realized in 1T-TaS₂/2H-TaS₂ bilayers where 1T-TaS₂ is a Mott insulator, and 2H-TaS₂ is a metal.⁴ STM experiments show a Kondo resonance in the tunneling spectrum appearing at around 27K.⁴ Similarly, synthetic Kondo lattices may be constructed in 2D magnet-metal/semimetal bilayers. As an example, a Kondo model with Kitaev intralayer interactions has been proposed for graphene/ α -RuCl₃ bilayers.⁵ Recent experimental and theoretical studies show that the interaction between graphene and α -RuCl₃ can have a significant impact on the electronic and magnetic properties of both layers.⁶⁻¹³

Compared to intermetallics, 2D vdW materials offer a broader tunability through gating, electric field, pressure, and strain.¹⁴ Their properties can be further controlled by twisting in

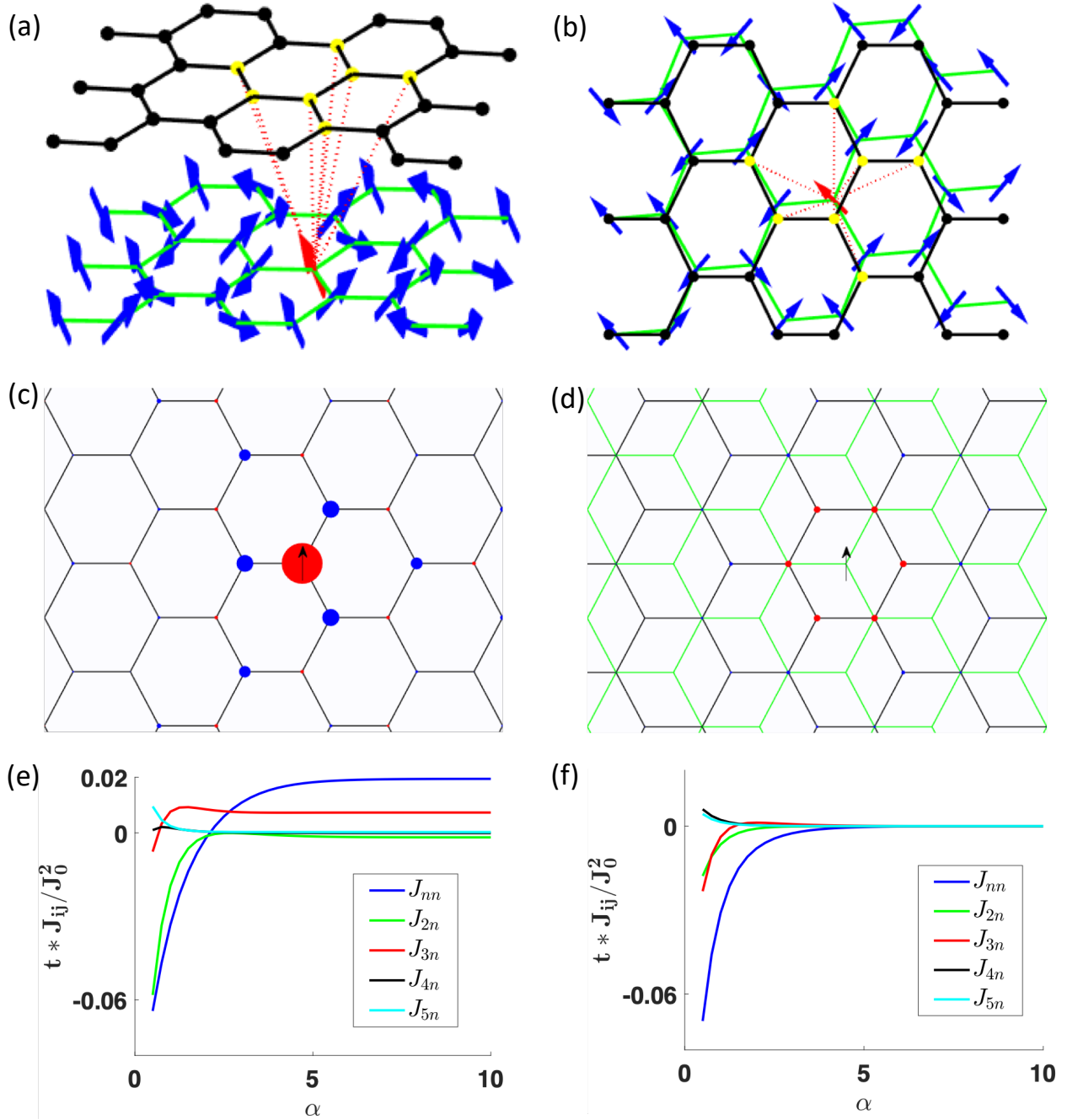


Figure 1: (a) Schematic representation of our model with conduction electrons on the upper layer and localized magnetic impurities on the lower layer, twisted relative to the upper layer. The magnetic impurity, indicated by the red arrow, interacts only with the conduction electrons at the sites shown in yellow in the conduction layer. (b) Top view of our schematic. (c), (d) Induced spin polarization for AA and AB stacking respectively for the inverse decay length $\alpha = 3$. The impurity spin is marked with black arrow and the area of the circles on each site is proportional to the spin polarization, where excess spin- \uparrow (spin- \downarrow) density is blue(red). (e), (f) The RKKY coupling, J as a function of α for AA and AB stacking up to fifth nearest neighbor.

moiré superlattices.¹⁵ A lattice mismatch in heterobilayers can also form moiré superlattices, even without twisting. For instance, the in-plane lattice constant of 1T-TaS₂ and 2H-TaS₂ are 3.36Å and 3.316Å respectively,^{16,17} which results in a moiré pattern with a periodicity of $L \sim 75$ unit cells.

Motivated by these recent developments, we develop a model to study the magnetic order in synthetic Kondo moiré superlattices. We consider honeycomb lattices for both layers and an extended Kondo interaction since the local stacking order changes within the moiré unit cell. In the limit of small twist angles, only a few sites are aligned perfectly on top of each other, corresponding to AA and AB stacking regions. For small twist angles, we calculate the Ruderman-Kittel-Kasuya-Yosida (RKKY) interaction^{18–20} via exact diagonalization up to third nearest neighbor and perform Monte Carlo simulations on the effective spin model to obtain the ground state spin texture. Our main results are as follows: (i) we show that the sign and the magnitude of the RKKY interaction varies depending on the local stacking order. (ii) Our Monte Carlo simulations indicate that the AA stacking regions order antiferromagnetically (AFM), whereas the AB regions order ferromagnetically (FM). The remaining parts of the moiré unit cell form ferromagnetic chains that are coupled antiferromagnetically (FMC). (iii) The extent of these regions varies with the inverse decay length of the Kondo interaction, α . For small α , FMC dominates the majority of the moiré unit cell, whereas for large α , FM, AFM, and FMC domains coexist.

We start by introducing the extended Kondo lattice Hamiltonian, which describes the interactions between localized magnetic moments with the conduction electrons in the moiré unit cell.

$$H = -t \sum_{\langle ij \rangle \sigma} (c_{ai\sigma}^\dagger c_{bj\sigma} + \text{H.c.}) - \mu \sum_{is\sigma} c_{is\sigma}^\dagger c_{is\sigma} + \sum_{ij;\alpha\beta} J_K(r_{ij}) c_{i\alpha}^\dagger \boldsymbol{\sigma}^{\alpha\beta} c_{i\beta} \cdot \mathbf{S}_j \quad (1)$$

where $c_{si\sigma}^\dagger$ is the creation operator for conduction electrons in $s = \{a, b\}$ sublattice and \mathbf{S} is the spin operator of the local moments. r_{ij} represents the distance between two sites,

$r_{ij} = |\mathbf{r}_i - \mathbf{r}_j|$. We consider the an extended Kondo coupling given by,

$$\begin{aligned} J_K(r_{ij}) &= J_0 e^{-\alpha r_{ij}/a_0} \text{ for } r_{ij} \leq \sqrt{3}a_0 \\ &= 0 \text{ otherwise.} \end{aligned} \tag{2}$$

where a_0 is the bond length on the honeycomb lattice and α is the inverse decay length. The cut-off in the exchange coupling for $r_{ij} > \sqrt{3}a_0$ is imposed for practical computational purposes.²¹ For the rest of the manuscript, we consider $\mu = 0$, a semimetallic filling for the conduction electrons and use $J_0/t = 10^{-2}$ to stay in the perturbative regime. Extended Kondo interaction is essential for the topological phases in heavy fermions.^{22–25} It has also been investigated for nematic²⁶ and higher angular momentum Kondo liquids.^{27,28}

RKKY interaction arises due to magnetic impurities interacting with conduction electrons which create net spin polarization. While the polarization propagates, it decays and undergoes Friedel oscillations. In Fig. 1(c), we present the spin polarization when the magnetic impurity is perfectly aligned on top of a conduction site (AA stacking). The polarization is antiferromagnetic to the magnetic impurity due to the nature of the Kondo exchange coupling. The coupling flips sign at its nearest neighbors (NN) due to the large Dirac momentum (short wavelength) Friedel oscillations, similar to the effect of magnetic impurities in graphene.²⁹ In Fig. 1(d), the magnetic impurity is placed at the center of the honeycomb (AB stacking). Note that the polarization is much smaller in this case since the local moment can only interact with conduction electrons at a distance $r = a_0$ and $J_K(r = a_0) \ll J_K(r = 0)$. The interaction of a second impurity with the spin-polarization induced by the first impurity leads to an effective interaction between the two local moments, which is known as RKKY interaction. In the absence of spin-orbit coupling, the RKKY interaction has SU(2) symmetry and can be expressed as a Heisenberg interaction, $J_{ij} \mathbf{S}_i \cdot \mathbf{S}_j$. We estimate the RKKY coupling constant via exact diagonalization following the procedure described in Ref. 29. We place two local moments at sites i and j and calculate the energy, including the interac-

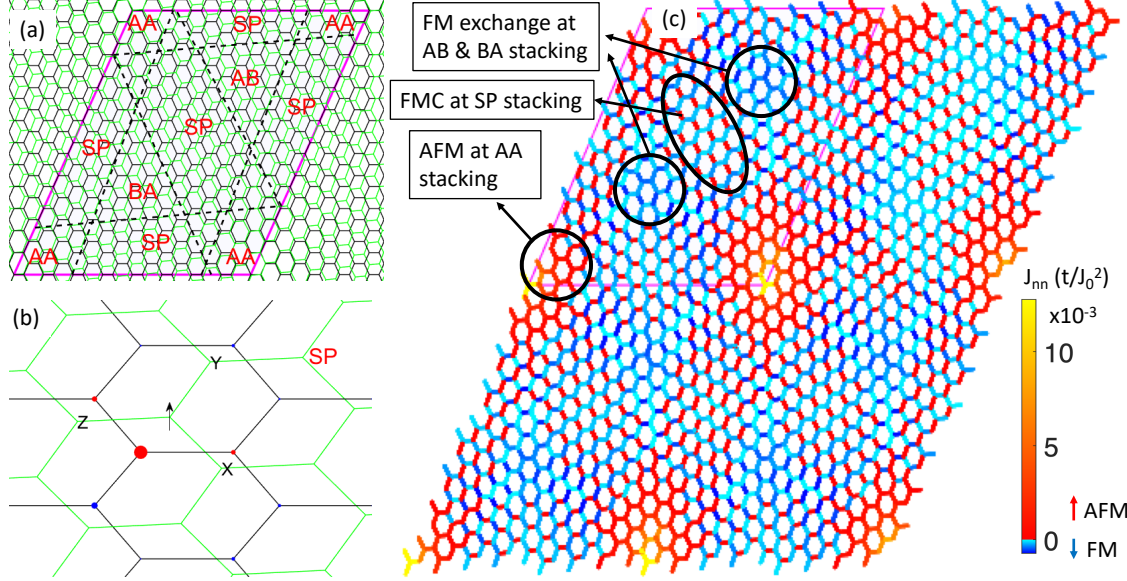


Figure 2: (a) Different stacking regions within a moiré unit cell: AA, AB, BA and saddle point (SP). (b) Conduction electron polarization induced by local moment for SP region for $\alpha = 4.6$. (c) NN RKKY interaction within a 2x2 moiré unit cell. Note that the dominant interaction is FM (AFM) for AB and BA (AA) regions. The SP regions 2 of the 3 bonds are FM and the remaining bond is AFM which results in FM chains that are coupled anti-ferromagnetically.

tions with the conduction electrons by aligning local moments parallel (E_{FM}) or antiparallel (E_{AFM}). The RKKY coupling is given by the energy difference, $J_{ij} = (E_{FM} - E_{AFM})/2S^2$. In the following, we consider unit spins, $S = 1$.

There are two key factors in determining the sign and the magnitude of the RKKY interaction, and both depend on the local stacking pattern. The magnitude of the RKKY interaction is primarily determined by the magnitude of r_{ij} . Since $J_K(r_{ij})$ decays exponentially with r_{ij} (eq. 2), the RKKY interaction which is proportional to $[J_K(r_{ij})]^2$ is overall larger in AA stacking regions where $r_{ij}/a_0 \ll 1$ compared to AB stacking where $r_{ij}/a_0 \sim 1$ for one of the magnetic impurity. The sign of the interaction depends on whether the local moments primarily couple to the same or different conduction sites. Coupling to the same conduction site results in an FM RKKY interaction. Yet, if they couple to NN sites, the sign of the conduction electron polarization flips between the NN sites due to Friedel oscillations as discussed above and the RKKY interaction is AFM in this case. To illustrate these effects,

we present the RKKY interaction as a function of α for AA stacking and AB stacking for the ‘untwisted’ system in Fig. 1(e) and (f). For $\alpha \gg 1$, we recover the limit of local Kondo interaction where the exchange is only significant for $r_{ij}/a_0 \ll 1$. In particular, the AA stacking shows AFM NN and FM next nearest neighbor (NNN) interactions. These results are in agreement with previous estimations for RKKY interaction in graphene.²⁹ On the contrary, the exchange constants are significantly smaller for the AB stacking region since $J_K(r = a_0)$ diminishes for $\alpha \gg 1$. However, unlike AA stacking, the NN exchange is FM since the local moments couple to the same conduction site.

For small α , the behavior of the exchange couplings is more complex due to multiple channels of Kondo interaction interfering with each other.³⁰ In particular, we find that the sign of the NN interaction changes to FM for AA stacking for $\alpha < 2$ and several other exchange couplings seem to diverge for $\alpha < 1$. In order to keep $J_K(r = \sqrt{3}a_0)/J_K(r = 0)$ small and justify the cut-off at $r > \sqrt{3}a_0$, we only consider $\alpha \geq 3$ for the remainder of the paper. To the best of our knowledge, the decay length dependence of the interlayer Kondo interaction in vdW materials has not been studied extensively. Still, we anticipate that $3 \leq \alpha \leq 10$ provides a regime that covers a large parameter space.

For small twist angles, the local stacking within a moiré unit cell can be described by a translational shift, $\mathbf{r}(\mathbf{R}) \simeq \theta \hat{\mathbf{z}} \times \mathbf{R}$ where \mathbf{R} and \mathbf{r} are the position within the moiré unit cell and translational shift respectively.^{21,31} Therefore, a moiré unit cell with a large periodicity can be considered as a superposition of all possible stacking orders.³² We label the different regions in the moiré unit cell by the primary stacking orders,³³ AA, AB, BA, and saddle point stacking (SP) in Fig. 2(a). These regions exhibit different types of RKKY interactions. A local moment placed in AA or AB stacking regions polarizes the conduction electrons similar to the untwisted case as depicted in Fig. 1(c) and (d). As a result, the effective magnetic interactions in these regions are similar to the untwisted case but superimposed in real space. The polarization induced by a local moment in the saddle point (SP) region is shown in Fig. 2(b). It is noteworthy to emphasize that among the three NN sites, two of them

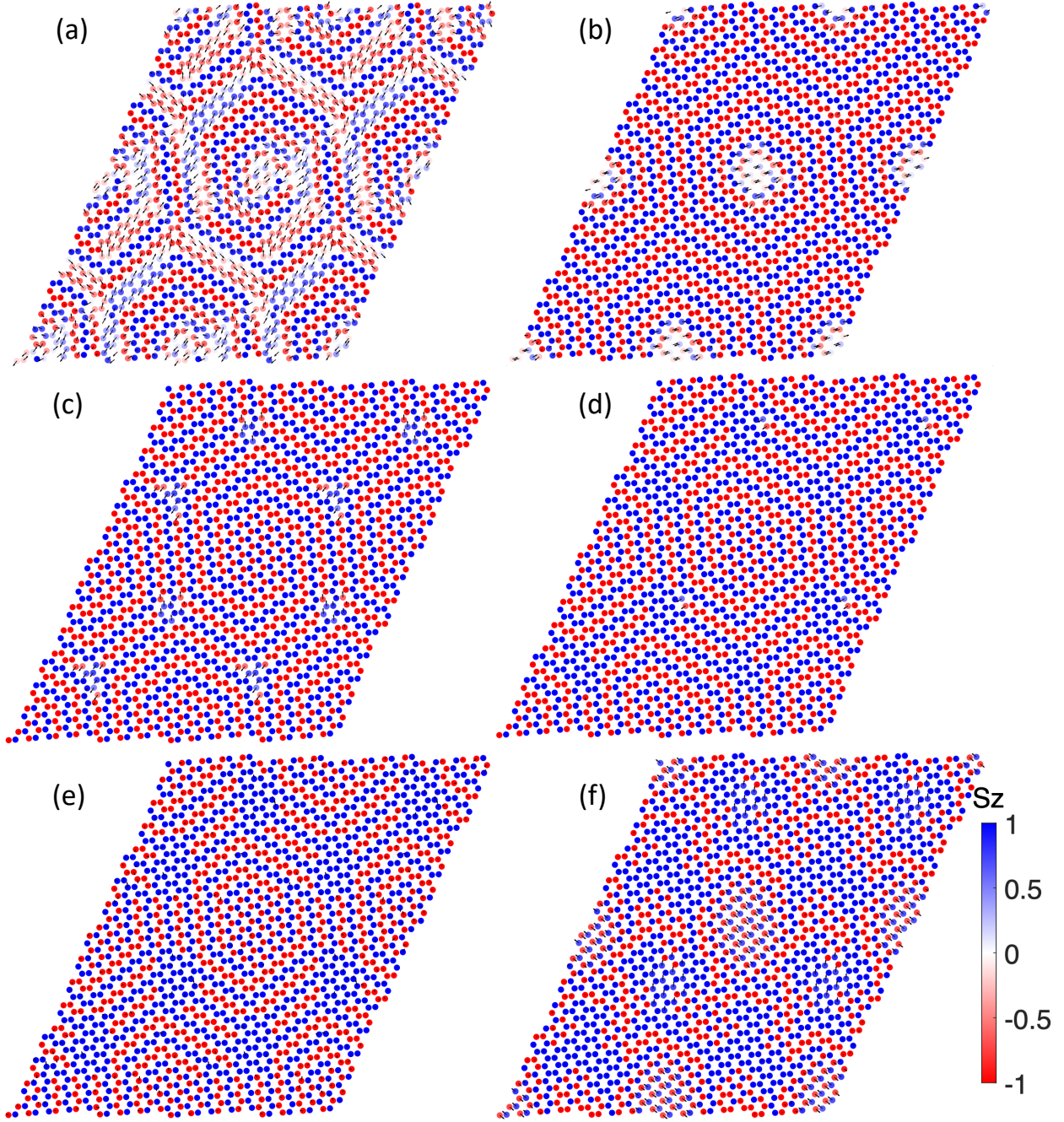


Figure 3: Monte Carlo snapshots for the ground state spin textures for $\alpha = 3, 3.2, 4.3, 4.6, 5, 10$ for (a)-(f) respectively. For $\alpha < 4$, the ground state primarily consists of ferromagnetic chains that are coupled antiferromagnetically with a small AFM region at the AA stacking. For $\alpha > 4$, FM (AFM) regions grow at AB and BA (AA) stacking regions within the moiré unit cell. The color plot shows the z-component of the magnetization, whereas the arrows show the in-plane component.

couple primarily to the same conduction site and therefore exhibit FM exchange. However, for the other bonds, the local moments couple to the different conduction sites, which results in AFM NN coupling. This leads to FM chains (FMC) in the SP region, as discussed below. We summarize these results in Fig. 2(c), where we present the NN exchanges for all the bonds within a 2×2 moiré unit cell for $\alpha = 4.6$. We consider a twist angle $\theta = 4^\circ$ with $N = 394$ unit cells for the remainder of the article, but our results are independent of the twist angle for small θ .

In order to determine the magnetic ground state of the moiré Kondo lattice, we derive the RKKY exchange couplings up to the third NN and perform classical Monte Carlo studies via the Metropolis algorithm. We include a small single site anisotropy term, $-J_A(S_i^z)^2$, which can naturally arise in real materials due to spin-orbit coupling,³⁴ to break the SU(2) symmetry of the model. We pick J_A much less than the smallest exchange coupling. Starting with random initial conditions, we perform 120,000 Monte Carlo updates at each temperature. We determine the ground state at $T/J_{\max} = 10^{-4}$ where J_{\max} is the maximum exchange coupling. Fig. 3 depicts the Monte Carlo snapshots of the ground state spin configurations for different values of α . We demonstrate that for $\alpha < 4$, the ground state primarily consists of FMC throughout the moiré unit cell and a small fraction of AFM around the AA stacking regions. For $\alpha > 4$, the FMC starts to shrink and FM (AFM) regions grow around AB and BA (AA) regions. FMC regions almost fully disappear as depicted in Fig. 3(f) for $\alpha = 10$. Note that for such values of α , RKKY coupling essentially vanishes except for the AA stacking regions.

In order to quantify these trends, we calculate the magnetization, $\langle M^\alpha \rangle = \langle \frac{1}{N} \sum_i S_i^\alpha \rangle$, and the static spin structure factor $S(\mathbf{q}) = (1/N^2) \langle \sum_{\beta=x,y,x} | \sum_i S_i^\beta e^{-i\mathbf{q}\cdot\mathbf{r}_i} |^2 \rangle$ of the ground state. $S(\mathbf{q})$ exhibits peaks at $\mathbf{q} = (0, 0)$, $\{\pm\mathbf{b}_{1(2)}/2, \pm(\mathbf{b}_1 + \mathbf{b}_2)/2\}$, $\{\pm\mathbf{b}_{1(2)}, \pm(\mathbf{b}_1 + \mathbf{b}_2)\}$, where $\mathbf{b}_{1/2}$ are the reciprocal lattice vectors, corresponding to FM, FMC and AFM orders respectively (see Supporting Information for details). We present the amplitude of these peaks in Fig. 4(a). The $\mathbf{q} = (0, 0)$ component of $S(\mathbf{q})$ is the square of the magnetization as

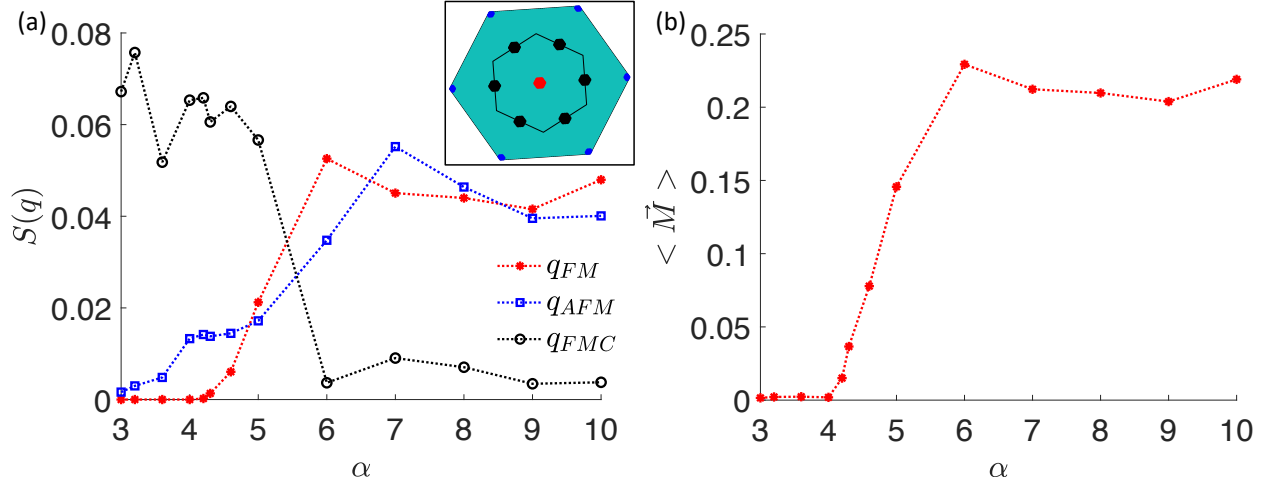


Figure 4: (a) Static spin structure factor $S(\mathbf{q})$ as a function of α , for $\mathbf{q} = (0,0)$ (red), $\mathbf{q} = \pm\mathbf{b}_1, \pm\mathbf{b}_2, \pm(\mathbf{b}_1 + \mathbf{b}_2)$ (blue) and $\mathbf{q} = \pm\mathbf{b}_1/2, \pm\mathbf{b}_2/2, \pm(\mathbf{b}_1 + \mathbf{b}_2)/2$ (black) corresponding to FM, AFM and FMC order respectively. The inset shows the position of these wave vectors in the extended Brillouin zone. (b) Net magnetization as a function of α . Note that the $\mathbf{q} = (0,0)$ component of the spin structure factor is the square of magnetization.

shown in Fig. 4(b). The spin structure factor also shows that the FMC is the primary order for $\alpha < 6$. For $\alpha > 6$, FMC regions shrink and AFM, FM regions grow rapidly. As shown in Fig. 4(b), the magnetization grows for $\alpha > 4$ and saturates at about $M/S = 0.2 - 0.25$.

Experimental detection of complex magnetic textures in the 2D limit is challenging. Although a variety of non-coplanar magnetic structures have been predicted in moiré superlattices of vdW magnets,^{31,32,35-45} only few of these phases have been observed experimentally by magnetic circular dichroism,⁴⁶ magneto-optical Kerr effect⁴⁷ and diamond NV magnetometry.⁴⁸ In particular, we expect that these techniques should be able to detect the FM domains.

In conclusion, we presented a theoretical framework for magnetic order in synthetic moiré Kondo lattices consisting of Mott insulator and metal vdW layers. We showed that the stacking-dependent Kondo interaction can give rise to various types of magnetic order. In particular, we demonstrated that the decay length of the Kondo interaction can control the magnetic textures. Interesting future directions include realistic simulations of material platforms, investigating the effects of pressure and gating, and the competition between

heavy fermion formation and magnetism in these systems.

Associated Content

Supporting Information

Details of the static spin structure factor calculation (pdf).

Author Information

Corresponding Author: Onur Erten – Email: onur.erten@asu.edu

Author Contributions: M. A. Keskiner have performed the exact diagonalization and Monte Carlo simulations. M. Ö. Oktel, Pouyan Ghaemi and Onur Erten have conceptualized the research. All authors have analyzed the results and contributed to writing the manuscript.

Notes: The authors declare no competing financial interest.

Acknowledgements

We thank Cemal Yalabik and Erik Henriksen for fruitful discussions. OE acknowledge support from National Science Foundation Award No. DMR 2234352. MAK and MOO are partially supported by TUBITAK 1001 grant No 122F346. PG acknowledges support from NSF DMR-2130544 and infrastructural support from NSF HRD-2112550 (NSF CREST Center IDEALS).

References

- (1) Stewart, G. R. Heavy-fermion systems. *Rev. Mod. Phys.* **1984**, *56*, 755–787.
- (2) Coleman, P. *Introduction to Many-Body Physics*; Cambridge University Press, 2015.

- (3) Wirth, S.; Steglich, F. Exploring heavy fermions from macroscopic to microscopic length scales. *Nature Reviews Materials* **2016**, *1*, 16051.
- (4) Ayani, C. G.; Pisarra, M.; Ibarburu, I. M.; Garnica, M.; Miranda, R.; Calleja, F.; Martin, F.; Vazquez de Parga, A. L. Probing the Phase Transition to a Coherent 2D Kondo Lattice. *Small* **2023**, 2303275.
- (5) Jin, H.-K.; Knolle, J. Flat and correlated plasmon bands in graphene/ α -RuCl₃ heterostructures. *Phys. Rev. B* **2021**, *104*, 045140.
- (6) Mashhadi, S.; Kim, Y.; Kim, J.; Weber, D.; Taniguchi, T.; Watanabe, K.; Park, N.; Lotsch, B.; Smet, J. H.; Burghard, M.; others Spin-split band hybridization in graphene proximitized with α -RuCl₃ nanosheets. *Nano letters* **2019**, *19*, 4659–4665.
- (7) Zhou, B.; Balgley, J.; Lampen-Kelley, P.; Yan, J.-Q.; Mandrus, D. G.; Henriksen, E. A. Evidence for charge transfer and proximate magnetism in graphene- α - RuCl₃ heterostructures. *Physical Review B* **2019**, *100*, 165426.
- (8) Biswas, S.; Li, Y.; Winter, S. M.; Knolle, J.; Valentí, R. Electronic Properties of α -RuCl₃ in proximity to graphene. *Physical Review Letters* **2019**, *123*, 237201.
- (9) Rizzo, D. J. et al. Charge-Transfer Plasmon Polaritons at Graphene/ α -RuCl₃ Interfaces. *Nano Letters* **2020**, *20*, 8438–8445.
- (10) Gerber, E.; Yao, Y.; Arias, T. A.; Kim, E.-A. Ab Initio Mismatched Interface Theory of Graphene on α - RuCl₃: Doping and Magnetism. *Physical Review Letters* **2020**, *124*, 106804.
- (11) Leeb, V.; Polyudov, K.; Mashhadi, S.; Biswas, S.; Valentí, R.; Burghard, M.; Knolle, J. Anomalous quantum oscillations in a heterostructure of graphene on a proximate quantum spin liquid. *Physical Review Letters* **2021**, *126*, 097201.

- (12) Balgley, J.; Butler, J.; Biswas, S.; Ge, Z.; Lagasse, S.; Taniguchi, T.; Watanabe, K.; Cothrine, M.; Mandrus, D. G.; Velasco Jr, J.; others Ultrasharp Lateral p–n Junctions in Modulation-Doped Graphene. *Nano Letters* **2022**, *22*, 4124–4130.
- (13) Shi, J.; MacDonald, A. Magnetic states of graphene proximitized Kitaev materials. *Physical Review B* **2023**, *108*, 064401.
- (14) Liu, Y.; Weiss, N. O.; Duan, X.; Cheng, H.-C.; Huang, Y.; Duan, X. Van der Waals heterostructures and devices. *Nature Reviews Materials* **2016**, *1*, 16042.
- (15) He, F.; Zhou, Y.; Ye, Z.; Cho, S.-H.; Jeong, J.; Meng, X.; Wang, Y. Moiré Patterns in 2D Materials: A Review. *ACS Nano* **2021**, *15*, 5944–5958.
- (16) Mattheiss, L. F. Band Structures of Transition-Metal-Dichalcogenide Layer Compounds. *Phys. Rev. B* **1973**, *8*, 3719–3740.
- (17) Clerc, F.; Bovet, M.; Berger, H.; Despont, L.; Koitzsch, C.; Gallus, O.; Patthey, L.; Shi, M.; Krempasky, J.; Garnier, M. G.; Aebi, P. Spin–orbit splitting in the valence bands of 1T-TaS₂ and 1T-TaSe₂. *Journal of Physics: Condensed Matter* **2004**, *16*, 3271.
- (18) Ruderman, M. A.; Kittel, C. Indirect Exchange Coupling of Nuclear Magnetic Moments by Conduction Electrons. *Phys. Rev.* **1954**, *96*, 99–102.
- (19) Yosida, K. Magnetic Properties of Cu-Mn Alloys. *Phys. Rev.* **1957**, *106*, 893–898.
- (20) Kasuya, T. A Theory of Metallic Ferro- and Antiferromagnetism on Zener’s Model. *Progress of Theoretical Physics* **1956**, *16*, 45–57.
- (21) Akram, M.; Kapeghian, J.; Das, J.; Valentí, R.; Botana, A. S.; Erten, O. Theory of Moiré Magnetism in Twisted Bilayer α -RuCl₃. *Nano Letters* **2024**, *24*, 890–896.
- (22) Dzero, M.; Xia, J.; Galitski, V.; Coleman, P. Topological Kondo Insulators. *Annual Review of Condensed Matter Physics* **2016**, *7*, 249–280.

- (23) Alexandrov, V.; Coleman, P.; Erten, O. Kondo Breakdown in Topological Kondo Insulators. *Phys. Rev. Lett.* **2015**, *114*, 177202.
- (24) Ghazaryan, A.; Nica, E. M.; Erten, O.; Ghaemi, P. Shadow surface states in topological Kondo insulators. *New Journal of Physics* **2021**, *23*, 123042.
- (25) Lai, H.-H.; Greife, S. E.; Paschen, S.; Si, Q. Weyl–Kondo semimetal in heavy-fermion systems. *Proceedings of the National Academy of Sciences* **2018**, *115*, 93–97.
- (26) Vijayvargia, A.; Erten, O. Nematic heavy fermions and coexisting magnetic order in CeSiI. 2024.
- (27) Ghaemi, P.; Senthil, T. Higher angular momentum Kondo liquids. *Phys. Rev. B* **2007**, *75*, 144412.
- (28) Ghaemi, P.; Senthil, T.; Coleman, P. Angle-dependent quasiparticle weights in correlated metals. *Phys. Rev. B* **2008**, *77*, 245108.
- (29) Black-Schaffer, A. M. RKKY coupling in graphene. *Phys. Rev. B* **2010**, *81*, 205416.
- (30) Ahamed, S.; Moessner, R.; Erten, O. Why rare-earth ferromagnets are so rare: Insights from the p -wave Kondo model. *Phys. Rev. B* **2018**, *98*, 054420.
- (31) Akram, M.; LaBollita, H.; Dey, D.; Kapeghian, J.; Erten, O.; Botana, A. S. Moiré Skyrmions and Chiral Magnetic Phases in Twisted CrX₃ (X = I, Br, and Cl) Bilayers. *Nano Letters* **2021**, *21*, 6633–6639.
- (32) Akram, M.; Erten, O. Skyrmions in twisted van der Waals magnets. *Phys. Rev. B* **2021**, *103*, L140406.
- (33) McGilly, L. J. et al. Visualization of moiré superlattices. *Nature Nanotechnology* **2020**, *15*, 580–584.

- (34) Banerjee, S.; Rowland, J.; Erten, O.; Randeria, M. Enhanced Stability of Skyrmions in Two-Dimensional Chiral Magnets with Rashba Spin-Orbit Coupling. *Phys. Rev. X* **2014**, *4*, 031045.
- (35) Tong, Q.; Liu, F.; Xiao, J.; Yao, W. Skyrmions in the moiré of van der Waals 2D Magnets. *Nano Letters* **2018**, *18*, 7194–7199.
- (36) Hejazi, K.; Luo, Z.-X.; Balents, L. Noncollinear phases in moiré magnets. *Proceedings of the National Academy of Sciences* **2020**, *117*, 10721–10726.
- (37) Hejazi, K.; Luo, Z.-X.; Balents, L. Heterobilayer moiré magnets: Moiré skyrmions and commensurate-incommensurate transitions. *Phys. Rev. B* **2021**, *104*, L100406.
- (38) Xiao, F.; Chen, K.; Tong, Q. Magnetization textures in twisted bilayer CrX₃ (X = Br, I). *Phys. Rev. Research* **2021**, *3*, 013027.
- (39) Xiao, F.; Chen, K.; Tong, Q. Magnetization textures in twisted bilayer CrX₃ (X=Br, I). *Phys. Rev. Res.* **2021**, *3*, 013027.
- (40) Ghader, D.; Jabakhanji, B.; Stroppa, A. Whirling interlayer fields as a source of stable topological order in moiré CrI₃. *Communications Physics* **2022**, *5*, 192.
- (41) Zheng, F. Magnetic Skyrmion Lattices in a Novel 2D-Twisted Bilayer Magnet. *Advanced Functional Materials* **2023**, *33*, 2206923.
- (42) Kim, K.-M.; Kiem, D. H.; Bednik, G.; Han, M. J.; Park, M. J. Ab Initio Spin Hamiltonian and Topological Noncentrosymmetric Magnetism in Twisted Bilayer CrI₃. *Nano Letters* **2023**, *23*, 6088–6094.
- (43) Fumega, A. O.; Lado, J. L. Moiré-driven multiferroic order in twisted CrCl₃, CrBr₃ and CrI₃ bilayers. *2D Materials* **2023**, *10*, 025026.
- (44) Nica, E.; Akram, M.; Vijayvargia, A.; Moessner, R.; Erten, O. Kitaev spin-orbital bilayers and their moiré superlattices. *npj Quantum Mater.* *8*, *9* **2023**,

- (45) Vijayvargia, A.; Nica, E. M.; Moessner, R.; Lu, Y.-M.; Erten, O. Magnetic fragmentation and fractionalized Goldstone modes in a bilayer quantum spin liquid. *Phys. Rev. Res.* **2023**, *5*, L022062.
- (46) Xu, Y.; Ray, A.; Shao, Y.-T.; Jiang, S.; Lee, K.; Weber, D.; Goldberger, J. E.; Watanabe, K.; Taniguchi, T.; Muller, D. A.; Mak, K. F.; Shan, J. Coexisting ferromagnetic–antiferromagnetic state in twisted bilayer CrI₃. *Nature Nanotechnology* **2021**,
- (47) Xie, H.; Luo, X.; Ye, Z.; Sun, Z.; Ye, G.; Sung, S. H.; Ge, H.; Yan, S.; Fu, Y.; Tian, S.; Lei, H.; Sun, K.; Hovden, R.; He, R.; Zhao, L. Evidence of non-collinear spin texture in magnetic moiré superlattices. *Nature Physics* **2023**,
- (48) Song, T.; Sun, Q.-C.; Anderson, E.; Wang, C.; Qian, J.; Taniguchi, T.; Watanabe, K.; McGuire, M. A.; Stöhr, R.; Xiao, D.; Cao, T.; Wrachtrup, J.; Xu, X. Direct visualization of magnetic domains and moiré; magnetism in twisted 2D magnets. *Science* **2021**, *374*, 1140–1144.

Supporting Information for “Theory of moiré magnetism and multi-domain spin textures in twisted Mott insulator - semimetal heterobilayers”

M. A. Keskiner,^{*,†} Pouyan Ghaemi,^{*,‡,¶} M. Ö. Oktel,^{*,†} and Onur Erten^{*,§}

[†]*Department of Physics, Bilkent University, Ankara, 06800, TURKEY*

[‡]*Physics Department, City College of the City University of New York, NY 10031, U.S.A.*

[¶]*Physics Program, Graduate Center of City University of New York, NY 10031, U.S.A.*

[§]*Department of Physics, Arizona State University, Tempe, AZ 85287, USA*

E-mail: akif.keskiner@bilkent.edu.tr; pghaemi@ccny.cuny.edu; oktel@fen.bilkent.edu.tr;
onur.erten@asu.edu

Details of the static spin structure factor calculation

In this section, we derive form of the spin structure factor for different spin textures including FM, AFM and FMC. In all cases, we assume that the broken symmetry axis is along the \hat{z} direction. We define the primitive lattice vectors for the honeycomb lattice as $\mathbf{a}_1 = \frac{3}{2}\hat{x} + \frac{\sqrt{3}}{2}\hat{y}$ and $\mathbf{a}_2 = \frac{3}{2}\hat{x} - \frac{\sqrt{3}}{2}\hat{y}$ shown in Fig. 1(a) (in units of bond length $a_0 = 1$). The corresponding reciprocal lattice vectors are $\mathbf{b}_1 = \frac{2\pi}{3}\hat{x} + \frac{2\pi}{\sqrt{3}}\hat{y}$ and $\mathbf{b}_2 = \frac{2\pi}{3}\hat{x} - \frac{2\pi}{\sqrt{3}}\hat{y}$ shown in Fig. 1(c).

We consider, $S_z^A = S_z^B = 1$ for FM and $S_z^A = -S_z^B = 1$ for AFM and calculate the spin

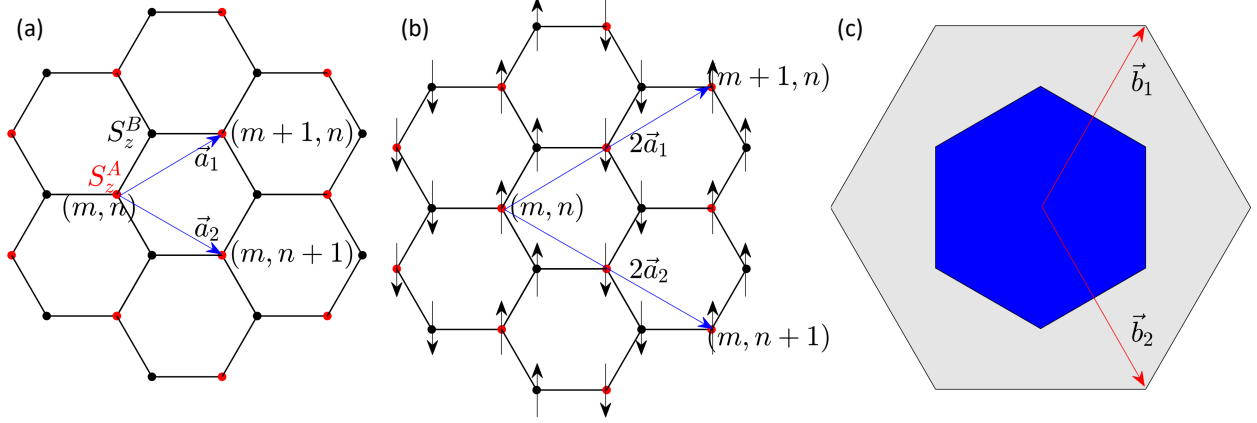


Figure 1: (a) Primitive vectors for the honeycomb lattice. (m, n) are integers and define the position of the site. If $S_z^A = S_z^B = 1$ and $S_{x-y}^{A(B)} = 0$ we have ferromagnetic order. If $S_z^A = -S_z^B = 1$ and $S_{x-y}^{A(B)} = 0$ we have antiferromagnetic order. (b) Ferromagnetic chain order in the zig-zag direction and primitive vectors defining unit cell in this ordering. (c) Reciprocal lattice with reciprocal lattice vectors. The blue region is the first Brillouin zone,

structure factor as follows,

$$\begin{aligned}
S(\mathbf{q}) &= (1/N^2) \langle |\sum_{m,n} S_z^A e^{i\mathbf{q}\cdot\mathbf{r}_{mn}} + S_z^B e^{i\mathbf{q}\cdot(\mathbf{r}_{mn} + \frac{1}{2}\hat{x} + \frac{\sqrt{3}}{2}\hat{y})}|^2 \rangle \quad (1) \\
&= \langle |\frac{1}{N} \sum_{m,n} e^{i\mathbf{q}\cdot\mathbf{r}_{mn}}|^2 \rangle \{ (S_z^A)^2 + (S_z^B)^2 + 2S_z^A S_z^B \cos(\frac{1}{2}q_x + \frac{\sqrt{3}}{2}q_y) \} \\
&= \delta_{\mathbf{q}, k_1\mathbf{b}_1 + k_2\mathbf{b}_2} \{ (S_z^A)^2 + (S_z^B)^2 + 2S_z^A S_z^B \cos(\frac{1}{2}q_x + \frac{\sqrt{3}}{2}q_y) \}
\end{aligned}$$

where $\mathbf{r}_{mn} = m\mathbf{a}_1 + n\mathbf{a}_2$ and $\{k_1, k_2, m, n\} \in \mathcal{Z}$. For FM ordering, the maximum value of $S(\mathbf{q})$ is at the point $\mathbf{q} = (0, 0)$, whereas for antiferromagnetic ordering, $S_z^A = -S_z^B = 1$, the maximum value of $S(\mathbf{q})$ is at the points $\mathbf{q} = \pm\{\mathbf{b}_1, \mathbf{b}_2, (\mathbf{b}_1 + \mathbf{b}_2)\}$ in the region shown in Fig. 1(c).

For FMC, the lattice vectors defining the unit cell are $2\mathbf{a}_1$ and $2\mathbf{a}_2$ (see Fig. 1(b)). There

are eight sites in the unit cell and the spin structure factor is

$$\begin{aligned}
S(\mathbf{q}) &= (1/N^2) \langle | \sum_{m,n} e^{i\mathbf{q}\cdot\mathbf{r}_{mn}} + e^{i\mathbf{q}\cdot(\mathbf{r}_{mn}+\frac{1}{2}\hat{x}+\frac{\sqrt{3}}{2}\hat{y})} + e^{i\mathbf{q}\cdot(\mathbf{r}_{mn}+3\hat{x})} + e^{i\mathbf{q}\cdot(\mathbf{r}_{mn}+\frac{7}{2}\hat{x}+\frac{\sqrt{3}}{2}\hat{y})} \\
&\quad - e^{i\mathbf{q}\cdot(\mathbf{r}_{mn}+\frac{3}{2}\hat{x}+\frac{\sqrt{3}}{2}\hat{y})} - e^{i\mathbf{q}\cdot(\mathbf{r}_{mn}+2\hat{x}+\sqrt{3}\hat{y})} - e^{i\mathbf{q}\cdot(\mathbf{r}_{mn}+2\hat{x})} - e^{i\mathbf{q}\cdot(\mathbf{r}_{mn}+\frac{3}{2}\hat{x}-\frac{\sqrt{3}}{2}\hat{y})} |^2 \rangle \\
&= \langle | \frac{1}{N} \sum_{m,n} e^{i\mathbf{q}\cdot\mathbf{r}_{mn}} |^2 \rangle \{ 16 \sin^2(\frac{3}{4}q_x - \frac{\sqrt{3}}{4}q_y) (\sin(\frac{1}{2}q_x) + \sin(q_x + \frac{\sqrt{3}}{2}q_y))^2 \} \\
&= \delta_{\mathbf{q}, \frac{k_1}{2}\mathbf{b}_1 + \frac{k_2}{2}\mathbf{b}_2} \{ 16 \sin^2(\frac{3}{4}q_x - \frac{\sqrt{3}}{4}q_y) (\sin(\frac{1}{2}q_x) + \sin(q_x + \frac{\sqrt{3}}{2}q_y))^2 \}
\end{aligned} \tag{2}$$

where $\mathbf{r}_{mn} = 2m\mathbf{a}_1 + 2n\mathbf{a}_2$ and $\{k_1, k_2, m, n\} \in \mathcal{Z}$. The maximum value of $S(\mathbf{q})$ occurs at the points $\mathbf{q} = \pm(\mathbf{b}_1 + \mathbf{b}_2)/2$ in the region shown in Fig. 1(c) for the zigzag direction. Due to C_3 symmetry, for the ferromagnetic chain orders in the other directions the maximum values appears at the points $\mathbf{q} = \pm\{\mathbf{b}_1/2, \mathbf{b}_2/2\}$.